Submesoscale variability on the edge of Kuroshio-shed eddy in the northern South China Sea observed by underwater gliders

Haiyuan Yang[1,2] · Zhiyuan Gao[1] · Ke Ma[1] · Zhaohui Chen[1,2] · Yanhui Wang[2,3] · Zhiyou Jing[4] · Xin Ma[1,2] · Wendong Niu[3]

Abstract

Based on a submesoscale-resolving glider observation from April 25 to May 4, 2018, characteristics and underlying dynamics of submesoscale variability at the edge of an anticyclonic eddy shed from Kuroshio in the Northern South China Sea are explored in this study. Three underwater gliders traveled across the frontal zone and implemented ∼ 300 dives, covering a horizontal distance of ∼ 160 km and a vertical depth of ∼ 500 m in 9 days. The character of k^{-2} slope for spectral potential energy and the strong lateral buoyancy gradient indicate frontogenesis-induced submesoscale motions on the eddy edge. Further analysis focusing on the potential vorticity and balanced Richardson number reveals the development of symmetric instability (SI), which is associated with the strong lateral gradient of buoyancy at the edge of the anticyclonic eddy in the late spring.

Keywords Kuroshio eddy shedding · Submesoscale variability · South China Sea · Underwater glider observation · Symmetric instability · Baroclinic instability

1 Introduction

Kuroshio, the western boundary current in the North Pacific, originates from the bifurcation of the North Equatorial Current (NEC). When flowing northward and passing by the Luzon Strait (LS), it loses the constraint of land and frequently sheds anticyclonic eddies (AEs) into the South China Sea (SCS) (Yuan et al. 2006; Wang et al. 2008). The AEs shed from Kuroshio account for 60% of the AEs in north SCS and thus have a prominent impact on the

Haiyuan Yang and Zhiyuan Gao contribute equally to this work.

✉ Zhaohui Chen
chenzhaohui@ouc.edu.cn

1 Frontier Science Center for Deep Ocean Multispheres and Earth System (FDOMES) and Physical Oceanography Laboratory, Ocean University of China, 238 Songling Road, Qingdao 266100, China

2 Laoshan Laboratory, Qingdao, China

3 Key Laboratory of Mechanism Theory and Equipment Design of Ministry of Education, Tianjin University, Tianjin, China

4 State Key Laboratory of Tropical Oceanography, South China Sea Institute of Oceanology, Chinese Academy of Sciences, Guangzhou, China

temperature, salinity, and momentum budget in the SCS (Chen et al. 2012; Nan et al. 2015; Zhang et al. 2017; Yang et al. 2019). After separating from the Kuroshio, the AEs move westward and eventually dissipate in the SCS. Previous studies found that a CE usually generated after the AE is shed from the Kuroshio (Nan et al. 2011; Zhang et al. 2016). Zhang et al. (2017) pointed that the CE generated from south of Taiwan due to strong barotropic instabilities leading by the large horizontal velocity shear. The wind effect (Sen et al. 2008), eddy-topography interaction (Nikurashin et al. 2013), loss of balance (Molemaker et al. 2005), and submesoscale processes (McWilliams 2021) are suggested to be important in eddy energy dissipation (Zhang et al. 2016). Among these processes, the role of submesoscale motions is rarely studied directly until now because of the limited observations. Compare to the quasi-geostrophic mesoscale processes, submesoscale motions are characterized by both Rossby number and Richardson number, bearing significant ageostrophic and non-stationary features which makes them hard to capture in ship-board observation (Munk et al. 2000; Thomas and Ferrari 2008; McWilliams 2016; Yu et al. 2019; Dong et al. 2020, 2021; Cao et al. 2021). The deformation front around the mesoscale eddy edge is an active submesoscale motions zone where prominent eddy energy transfers to small-scale turbulence through instability

(McWilliams 2021). Zhang et al. (2016) conducted the first synthetic observation of the shedding eddies by deploying mooring arrays in the north SCS. However, the horizontal resolution of these mooring arrays is far from resolving the submesoscale motions. By assuming that all of the increased submesoscale (whose period is shorter than 10 days in their study) energy originates from mesoscale motions, they indirectly estimated the eddy energy dissipation by submesoscale motions. The result indicated that over half of the eddy energy is dissipated by submesoscale motions at the eddy edge. However, this simplified energy cascade method remains a large uncertainty due to the complexity of the energy cascade between submesoscale and other processes (Garabato et al. 2022; Taylor and Thompson 2023). Using field observation data of three warm eddies in the north SCS, Yang et al. (2017) reported elevated dissipation in the surface mixed layer near the eddy periphery and attributed this to submesoscale processes associated with mixed layer instability. Their conclusion was subsequently supported by Dong et al. (2022), who compared observed dissipation with calculated contribution from the parameterization of different instability processes in winter. However, the mixed layer depth in the SCS has a strong seasonal cycle, exceeding 70 m in winter and falling below 20 m in summer (Qu et al. 2007). Thus, the mixed layer instability may not work in triggering submesoscale motions in the late spring or early summer when the mixed layer is shallow in the SCS. Therefore, the leading mechanism for the generation of submesoscale motions in the late spring and early summer in the SCS needs to be further confirmed.

In addition to the non-stationary features, another reason for the scarcity of in situ observations of submesoscale motions in the SCS is the lacking of fast-sampling techniques (Zhong et al. 2017; Zhang et al. 2021). In the past decade, one of the revolutionary techniques for oceanic observations, i.e., the underwater gliders, was developed and began to be involved in recent submesoscale observations (Rudnick 2016; Thompson et al. 2016; Erickson and Thompson 2018; Swart et al. 2020). Using year-long time series recorded by gliders, Thompson et al. (2016) studied instabilities related to submesoscale dynamics in the Northeastern Atlantic. Subsequently, Erickson and Thompson (2018) reported evident carbon export through submesoscale instability. Another glider-based project reveals that submesoscale motions could regulate vertical stratification in the sub-Antarctic zone of the South Ocean (Swart et al. 2015; du Plessis et al. 2017). In addition to the ocean interior, Thomsen et al. (2016) investigated subduction led by submesoscale processes in the boundary upwelling system off Peru based on a glider. The application of underwater gliders in the global ocean makes it applicable in the SCS.

With the advantages of the gliders in its observation of submesoscale, we adopted three gliders to perform a submesoscale-resolving experiment from April 25 to May 4, 2018. Following previous studies (e.g., Thompson et al. 2016; Viglione et al. 2018), we further provide some in situ evidence for submesoscale activity at the eddy edge and related instability processes. The rest of this paper is organized as follows: Section 2 gives a brief description of the observations, datasets, and simulations used in this study. In Section 3, a detailed study of the submesoscale characteristics and associated instabilities is presented. This paper ends with a summary and further discussion in Section 4.

2 Data

2.1 Glider observations

Gliders were deployed around the edge of anticyclonic eddy (AE) shed from the Kuroshio to capture the submesoscale motions (Figs. 1 and 2). The absolute dynamic topography (ADT) data indicated that this AE origins from the meander of the Kuroshio in later spring (Fig. 1). At February 22, the Kuroshio intruded the north SCS and occurred loop current. At February 26, the AE shed from the Kuroshio and move westward. Adjacent with the AE, a cyclonic eddy (CE) is produced in the southeast of the AE, which may due to the barotropic instability (Zhang et al. 2017). At April 25, the AE moved at the 113°E with weaker magnitude than when it just shed form the Kuroshio. In the vicinity of the front between AE and CE, strong ocean current of 0.3 m/s and significant temperature gradients of 0.05 ℃/km appeared (Fig. 2).

Three gliders (PG, acronym for Petrel II Glider designed and manufactured by Tianjin University; please refer to Liu et al. (2017) for details) were deployed near the CE center (19°N, 115.2°E) and piloted westward over a period of 9 days (April 25–May 4, 2018). In order to gain high-resolution data, each glider was set to dive westerly from the surface to around 500 m as fast as possible. Figure 2b reveals that the observation covers the vicinity of boundary between AE and CE. All glider trajectories are roughly parallel and close to each other, but deflected from prescribed routes and slightly shifted toward the south owing to the background flow at the eastern edge of the AE. Equipped with SeaBird GPCTD, the gliders sampled every 1 s (~0.4 m vertically) and collect temperature and salinity during descending ascending profiles. All of the data has been quality controlled by a series of methods and we selected the upward portion that contains more samplings with superior quality in the upper ocean (Garau et al. 2011). In addition, the top 10-m segment in each profile is discarded because of discontinuous series in horizontal. At the end of this experiment, PG1, PG2, and PG3 have completed 306, 285, and 314 valid dives, respectively. Each dive takes 38 ± 0.58 min

Fig. 1 Distributions of ADT between February 22 and April 25, 2018. Black lines are ADT contours for 1.1 m and 1.2 m. Each red box in the second to the last subfigure denote the AE shed from the Kuroshio
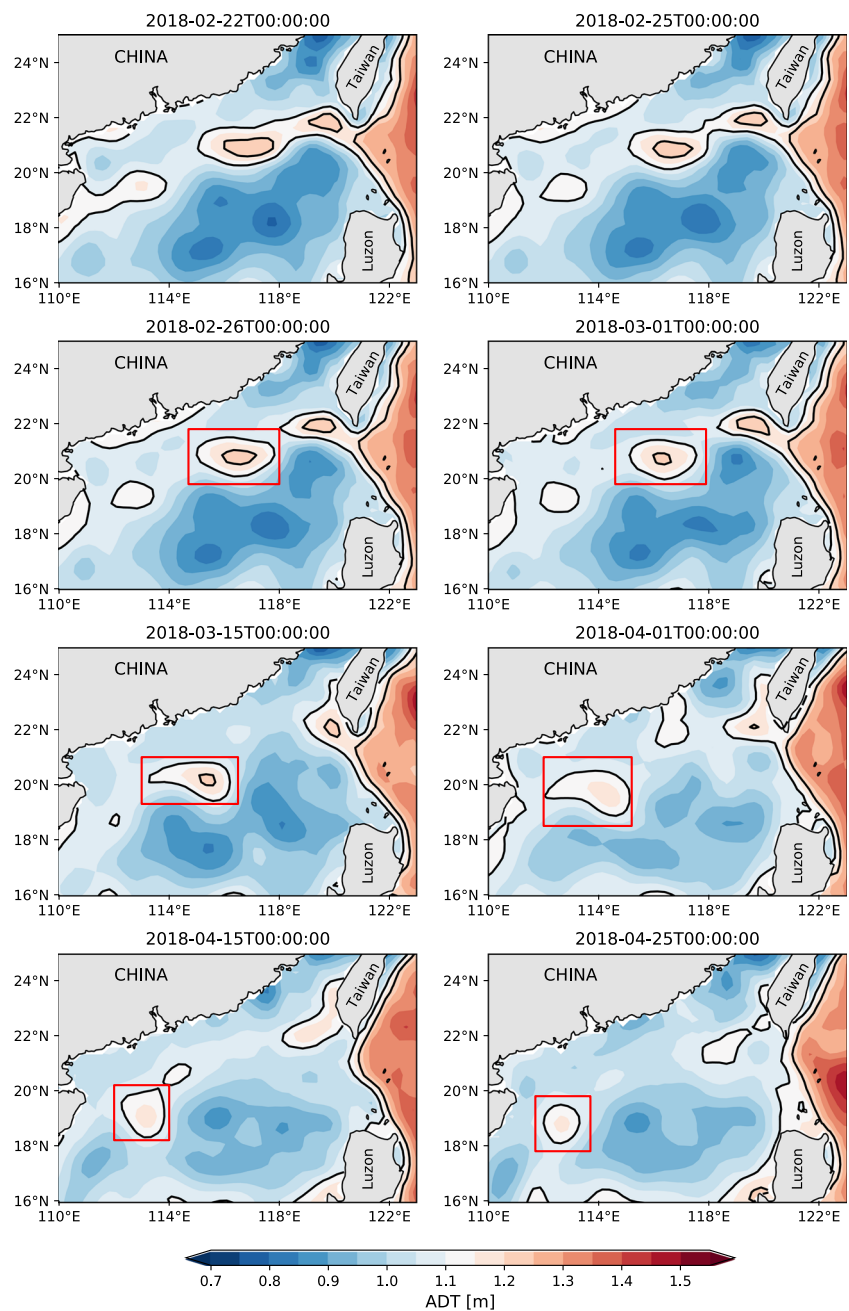
and spans 0.6 ± 0.17 km on average, which is sufficient for resolving submesoscale both temporally and spatially. For the analysis described below, especially the calculation of horizontal and vertical gradients, we interpolate temperature and salinity onto regular grids in depth and distance domains with vertical and horizontal resolutions of 1 m and 0.5 km. Each profile is treated as a vertical profile obtained at the position where the glider surfaced at the end of that dive. All the gliders are used for the spectral analysis while only PG1 data are used for calculating the instability and restratification processes because it had the straightest trajectory and collected a large number of profiles.

2.2 Observation and reanalysis products

Satellite observations are used to describe the background oceanic environment in this study. The 1/4° daily ADT, sea level anomaly (SLA), and geostrophic velocity data were derived from Copernicus Marine Environment Monitoring Service (CMEMS) L4 reprocessed dataset. The sea surface temperature (SST) product characterized by a resolution of 1 km is obtained from the Group for High-Resolution Sea Surface Temperature (GHRSST) L4 Multiscale Ultra-high Resolution (MUR) analysis. In addition to satellite, the hourly surface heat flux and wind stress taken from the
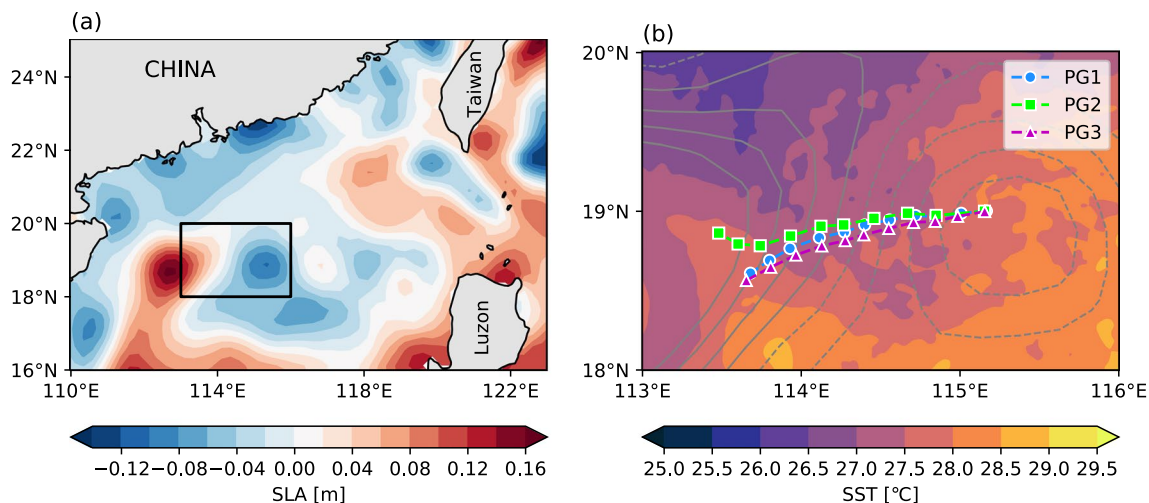
Fig. 2 **a** Sea level anomaly (SLA; shading) in the northern SCS on April 25. The box indicates the region of observation. **b** Sea surface temperature (SST; shading) and SLA (contours) on the same day in **a**. The blue, green, and red lines represent glider trajectories of PG1, PG2, and PG3, respectively. The dots on each trajectory mark the position of first dive on each day

European Centre for Medium-Range Weather Forecasts ERA-5 reanalysis data with $1/4° \times 1/4°$ horizontal resolution are used to evaluate the atmospheric forcing on submesoscale processes.

2.3 Model simulations

To support the results based on glider observation, a high-resolution nesting simulation in the SCS based on the Regional Oceanic Modeling System (ROMS; Shchepetkin and McWilliams 2005, 2011) was conducted. To coverage over the whole SCS basin, the domain of the parent simulation ROMS0 spans 2.5–25.5°N and 105–127°E, with a horizontal resolution of ~1.5 km (Fig. 3), while the child simulation ROMS1 was set to cover the northern SCS (15–24°N, 109.5–120.5°E; thick black box in Fig. 3) with a refined resolution of ~0.5 km. An online nesting approach is used between ROMS0 and ROMS1 in the same terrain-following S-Coordinate with 60 vertical levels. In the nesting simulation, the initial state and boundary conditions of ROMS0 are obtained from the monthly climatology of the Simple Ocean Data Assimilation (SODA) version 2.2.4. ROMS0 is

Fig. 3 Rate between relative vorticity and Coriolis parameter in the SCS on February 15, model year 23. The parent simulation ROMS0 was configured over the whole SCS basin (2.5–25.5°N, 105–127°E). The outer box presents the simulation region of ROMS1(15–24°N, 109.5–120.5°E), whereas the inner box gives the region of observation as in Fig. 2b
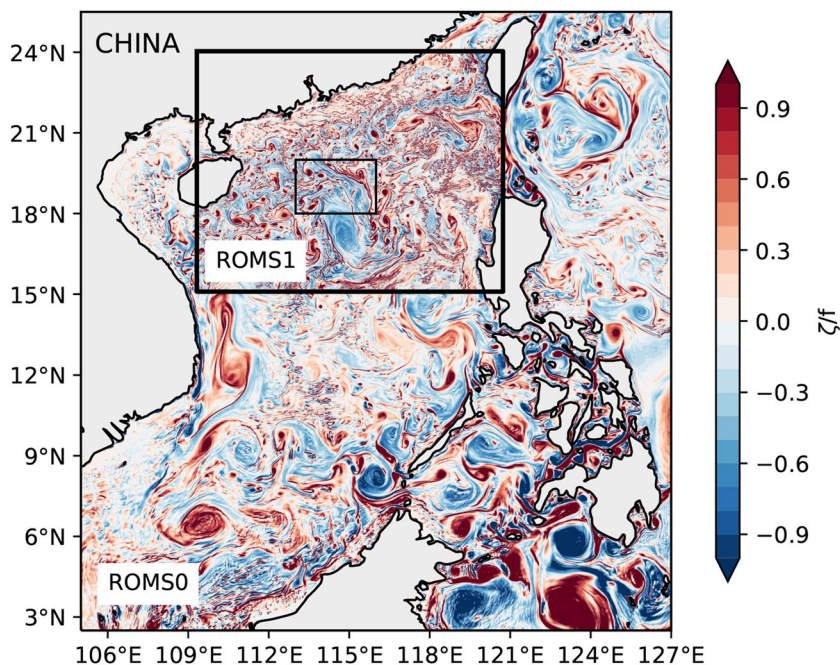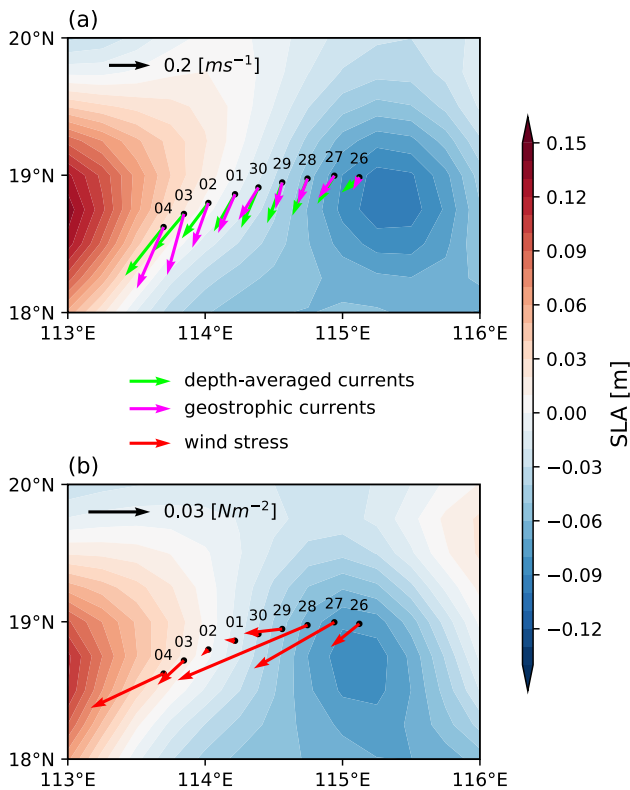
Fig. 4 SLA on **a** April 25 and **b** May 3. The lines represent trajectory of PG1 and the dots mark the position of the first dive on each day. The green and pink arrows denote are the depth-averaged currents and geostrophic currents derived from the glider's observation, respectively. The red arrows denote the wind stress derived from ERA 5 reanalysis data

spun up for 20 years forced by climatology monthly-mean heat and freshwater fluxes (the International Comprehensive Ocean–Atmosphere Data Set, ICOADS) and daily surface wind (the Quick Scatterometer, QuikSCAT) to reach the statistical equilibrium of total kinetic energy. Then, the model is running for additional years to acquire daily-mean outputs of ROMS1 for the diagnostic analysis.

3 Results

3.1 Characterization of submesoscale processes

Figure 4a and b show the SLA field in the observation region on April 25 and May 3, respectively. During our observation, the background current changes insignificantly, which maintains the stable existence of the frontal zone with both isotherms and isopycnals tilting down from east toward west (Fig. 4a and b). The mixed layer depth (MLD) is defined based on both temperature and density increments. The temperature threshold is 0.8 ℃, and the density threshold is equivalent to the change in density corresponding to the temperature threshold under constant salinity at the reference depth (Kara et al. 2000). The reference depth is chosen as 10 m to avoid surface disturbance and the results show a shallow MLD (~ 25 m) in the springtime SCS.

Figure 5 presents the along-track depth-averaged current, which is estimated by dead reckoning over the diving time (~ 36 min; the depth-averaged current does not include the drift while the glider is at the surface). Spectral analysis

Fig. 5 The eastward (**a**) and northward (**b**) components of depth-averaged current (blue), tide-removed current (black), and satellite-derived geostrophic current (grey). The bottom x-axis refers to the cumulative distance from the position where PG1 deployed, whereas the top x-axis is the date from the deployment. Noted that time and distance increase to the left not the right
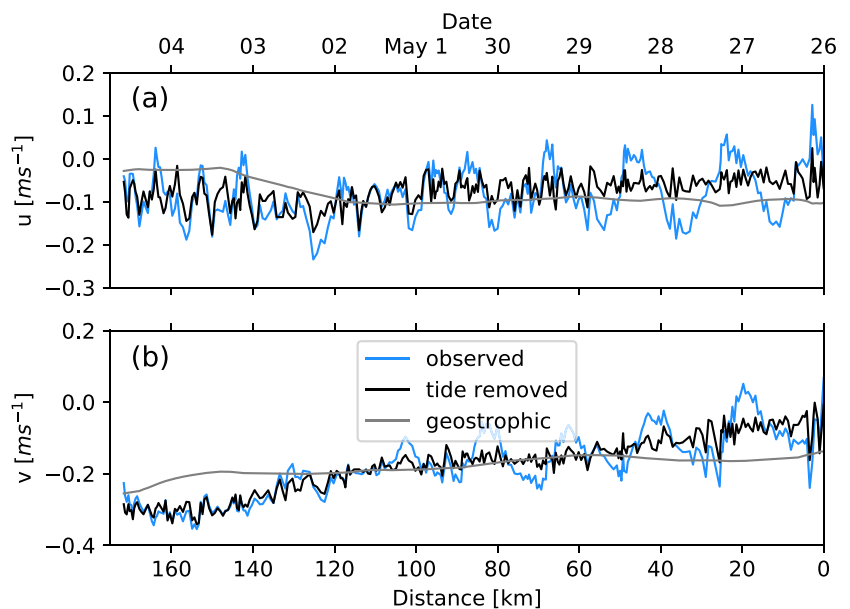
reveals that the current is characterized by 1-day and 0.5-day periodic signals associated with tides (not shown). To isolate the spatial distribution of observed factors from tidal effects, we adopt the moving harmonic analysis on gridded data at each depth (Johnston et al. 2013; Rainville et al. 2013). Principal constituents K_1, O_1, M_2, and S_2 are then subtracted at the midpoint of respective 33-h moving window. This method effectively removes internal tides and retains features at other scales (Fig. 6). Rudnick and Cole (2011) attributed this variability to Doppler smearing and aliasing, which could be eliminated by sampling quickly at higher resolution. Therefore, the required resolution needs to be smaller than ~0.5 km to avoid aliasing at the submesoscale wavelength. We have increased the spatial resolution through a fast-sampling strategy to minimize aliasing to the utmost extent. In this regard, we treat the fluctuation as the manifestation of physical processes in the ocean.

Compared to the geostrophic flow derived from altimeter, the tide-removed and depth-averaged glider velocity is characterized by a larger southward component when gliders bordered the frontal zone at May 03–04 (Fig. 4a), implying the ageostrophic nature of oceanic movement in that region. To further confirm this inference, discrete Fourier transform (DFT) is used to estimate spectral slopes of horizontal potential energy $P = b^2/(2N^2)$ in wavenumber space (Callies and Ferrari 2013). Here, $b = g(1-\rho/\rho_0)$ is buoyancy and N is background stratification, where g is gravity, ρ is density, and $\rho_0 = 1025$ kg·m^{-3} is the reference density. For each glider, we linearly interpolate quality-controlled data on equidistant grids to obtain gap-free spatial series at each depth. Then we remove the spatial mean and linear trend and perform DFT without tide-removed process. The spectra show similar magnitudes in the mixed layer and a depth of 200 m (Fig. 7). The slopes in the submesoscale range (2–20

Fig. 6 Along-track sections of **a** conservative temperature (Θ) and **b** absolute salinity (SA). The white lines denote mixed layer depth. **c** and **d** are the difference after tide-removed process. Noted that distance and time of x-axis increases to the left not the right, as per Fig. 5
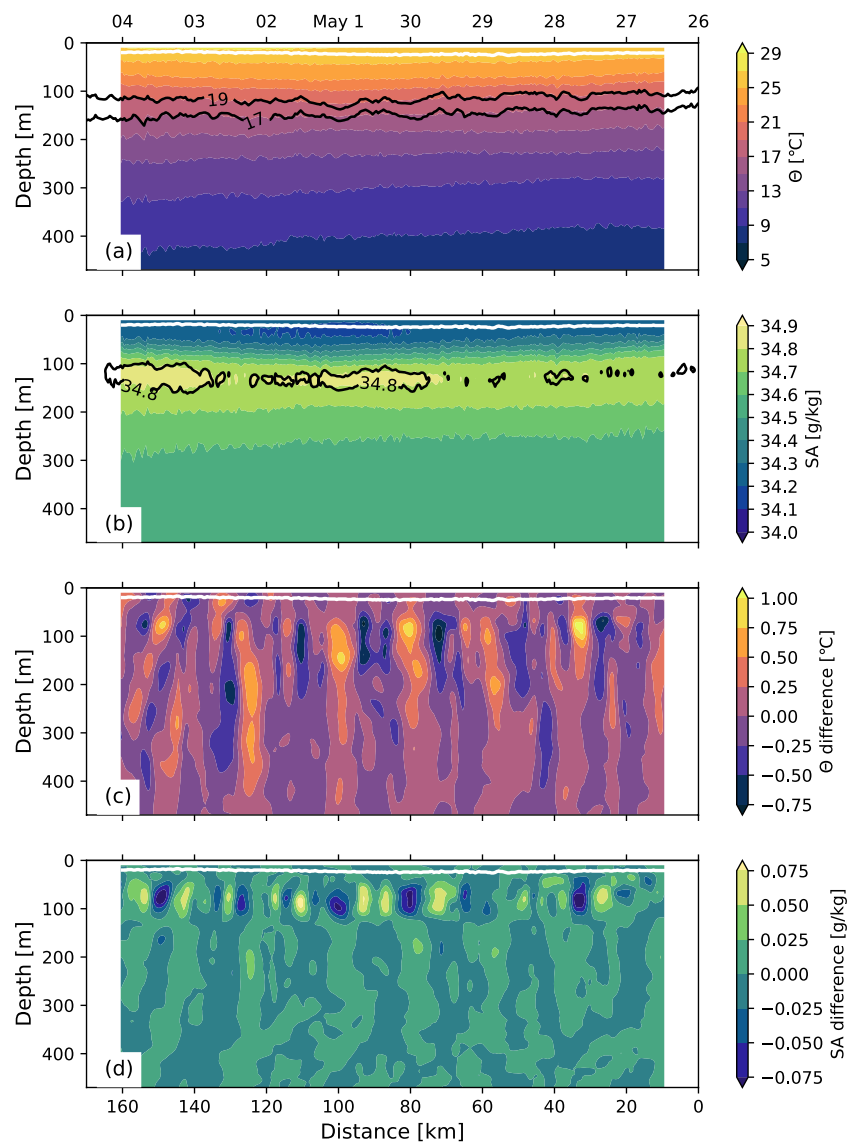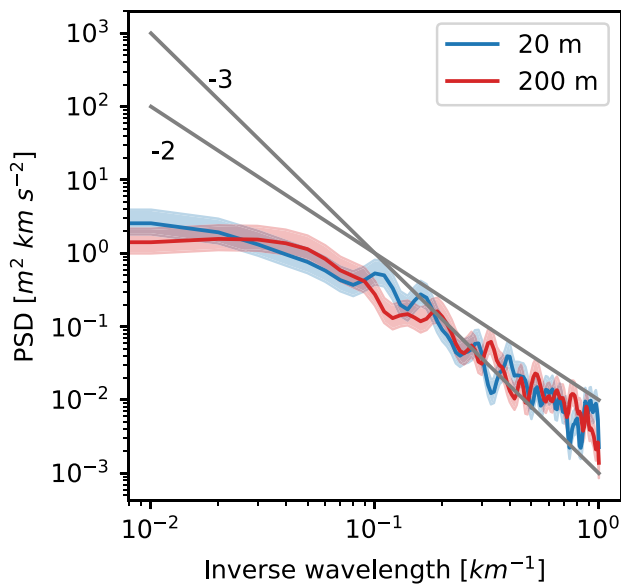
Fig. 7 Wavenumber spectra of horizontal potential energy of PG1 at the depth of 20 m (mixed layer depth) and 200 m. The shadings show 95% confidence levels

km) close to − 2 at both depths. The internal waves have rich energy in the SCS and the wavelengths span several to hundreds of kilometers depending on the modes. Callies and Ferrari ([2013](#)) interpret the energy and tracer spectra in the submesoscale range in the Eastern Pacific. In their work, the energy is significantly reduced in the mixed layer at scales below 20 km, which is to satisfy the zero-boundary condition. In this study, although no significantly reduced spectral magnitude in the mixed layer compared to the depth of 200 m, the spectra would also be influenced by strong internal waves. It is difficult to characterize the submesoscale spectral slope from the glider's data due to the inherent difficulty of eliminating internal waves from the observed data.

To verify the observed submesoscale spectra slope, we analyzed a nesting simulation. Model results denote a noticeable discrepancy in SST distribution between ROMS0 and ROMS1, with stronger and sharper fronts in the latter (Fig. 8a and b). The frontal structures between an eddy pair and filamentary features around the eddy periphery are indicative of submesoscale activity. Note that the magnitude of the sea level anomaly and the horizontal SST gradient are
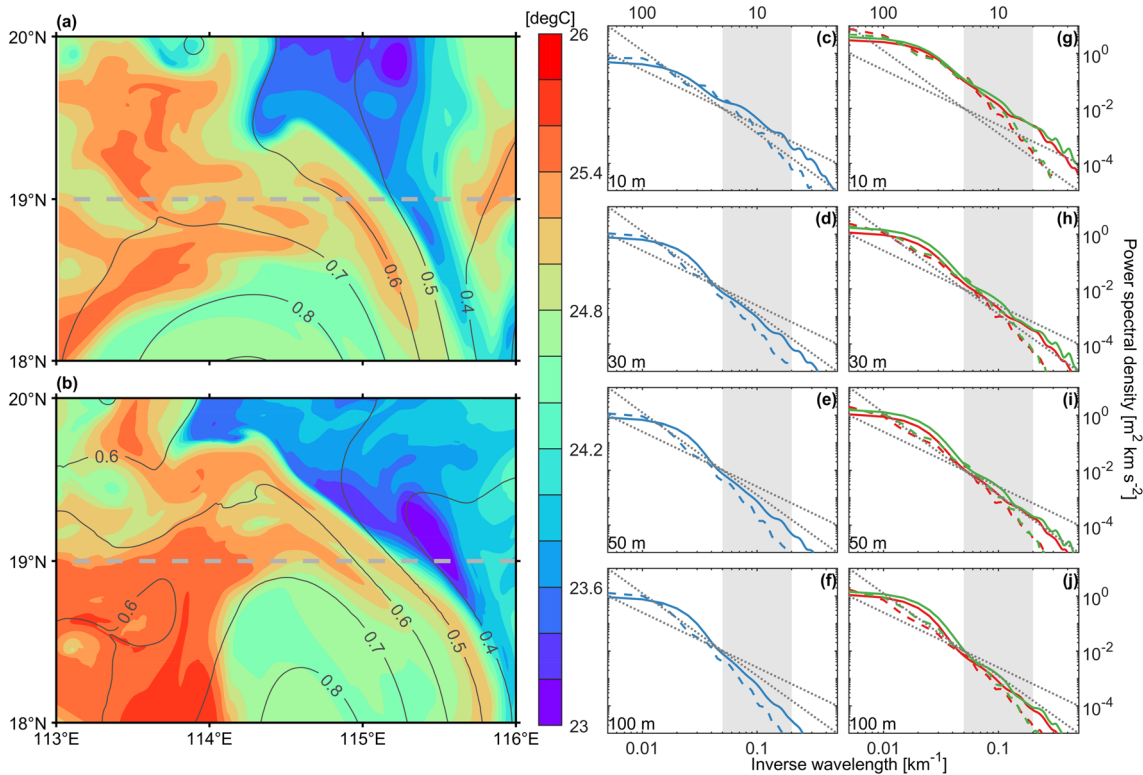

Fig. 8 SST (shading) overlaid with sea surface height (contours) on February 15 for **a** ROMS0 and **b** ROMS1. The gray line indicates the transect. The PSDs of potential energy **c** in the mixed layer, **d** at the base of the mixed layer, **e** in the thermocline, and **f** at the base of the thermocline. **g**–**j** The PSDs of along-track (red) and cross-track (green) kinetic energy at the corresponding depth in (**b**–**f**). The dashed and solid lines represent PSDs in ROMS0 and ROMS1, respectively. The submesoscale range (shading) is defined as 2–20 km in wavelength

consistent with the glider's observations. Thus, we emulate glider trajectories and select a transect across the frontal zone. Since the MLD in the SCS varies subtly between February and April (Zeng and Wang 2017), we select particular days (February 11–20, year 23) when field patterns are analogous to those during the observation period (Fig. 1b). Figure 8c–f illustrates the wavenumber spectra of potential energy at constant depths in the mixed layer, at the base of the mixed layer, in the thermocline and at the base of the thermocline, respectively. At scale larger than 20 km, the potential energy spectra in ROMS1 follow a k^{-3} power law at all depths and their energy is on the same order of magnitude. Within the submesoscale range, in comparison, the potential energy spectra scale close to k^{-2} in the mixed layer, then fall in between k^{-2} and k^{-3} at the base of the mixed layer and eventually roll off steeply in the thermocline. In ROMS0, the potential energy spectra shift generally to lower wavenumbers, with k^{-3} spectra in the whole mixed layer. Similar results can be extended to wavenumber spectra of kinetic energy except that spectral energy decays slightly from the mixed layer to the thermocline (Fig. 8g–j).

3.2 Instabilities and restratification processes

We use the methods of Thompson et al. (2016) to estimate PV and identify instability types. The methods are described in detail by Thompson et al. (2016) so we give only a summary here. Ertel PV is used as an indicator to characterize the potential for flow instabilities. Based on Hoskins (1974) and Thomas et al. (2013), instabilities can develop when PV takes the opposite sign of Coriolis parameter. The Ertel PV is defined as.

$$q_{\mathrm{Ertel}} = \omega_a \cdot \nabla b = (2\Omega + \nabla \times u) \cdot \nabla b = (f + \zeta)N^2 + (w_y - v_z)b_x + (u_z - w_x)b_y, \tag{1}$$

where ω_a is absolute vorticity, Ω is Earth's angular velocity, $\mathbf{u} = (u,v,w)$ is three-dimensional velocity vector, b is buoyancy, f is Coriolis parameter, $\zeta = v_x - u_y$ is vertical relative vorticity, $N^2 = b_z$ is vertical buoyancy gradient, and subscripts denote partial differentiation. Limited by the glider sampling capabilities, Thompson et al. (2016) simplified Eq. 1 to a two-dimensional expression by omitting negligible terms and assuming thermal wind balance

$$q_{\mathrm{Obs}} = (f + v_x)N^2 - \frac{b_x^2}{f}. \tag{2}$$

Here, x and y be the along-track and cross-track directions, respectively. It is noted that v_x cannot be estimated from the thermal wind relationship alone, thus we estimate the barotropic component of v using the depth-averaged current from the glider dives (Thompson et al. 2016). During our observation, v_x tends to be large when b_x is large and does not tend to change the period when $q_{\mathrm{Obs}} < 0$.

To explore when PV becomes negative and whether it is caused by changes in vertical or horizontal buoyancy gradients, Fig. 9 summarizes the evolution of b_x, b_z and PV derived from glider. In April 29, May 2, and May 3, b_x is found to be large, which represents the reservoirs of potential energy in the frontal zone (Fig. 9a). In comparison, stratification is stable but considerably weak throughout the observation period (Fig. 9b). As a consequence, the evolution of PV is dominated by b_x with three negative cases (Fig. 9c). The Frontogenesis function (F_{front}) was also examined (Thomas et al. 2013):

$$F_{front} = 2Q \cdot \nabla_h b, \tag{3}$$

where

$$Q = \left(-\frac{\partial \mathbf{u}}{\partial x} \cdot \nabla_h b, -\frac{\partial \mathbf{u}}{\partial y} \cdot \nabla_h b \right) \tag{4}$$

is the Q-vector (Hoskins 1982). Strong frontogenesis occurs in April 29, May 2, and May 3, which indicated the strong horizontal flow increased the lateral buoyancy gradient (Fig. 9d). In addition to PV, we further calculate the Rossby number (Ro $= \zeta/f$) and balanced Richardson number ($Ri_b = f^2 N^2/b_x^2$). It is found that Ro increases to 0.6 and Rib drops to 0.3 during the negative PV periods, indicating the ageostrophic characteristics and supporting the results of spectral analysis.

Following Thomas et al. (2013), we identify instability types by introducing the balanced Richardson angle, given by

$$\phi_{Ri_b} = \tan^{-1}\left(-Ri_b^{-1}\right). \tag{5}$$

In their Fig. 1, Thomas et al. (2013) showed schematically the range of angles associated with gravitational instability, a mixed gravitational and symmetric instability (SI), and SI. In particular, for stable stratification and cyclonic vorticity ($\zeta > 0$), the SI is the dominant mode of instability when

$$-\pi/2 < \phi_{Ri_b} < \phi_c < -\pi/4. \tag{6}$$

For anticyclonic vorticity ($\zeta < 0$), the SI forms when

$$-\pi/2 < \phi_{Ri_b} < -\pi/4 < \phi_c, \tag{7}$$

while

$$-\pi/4 < \phi_{Ri_b} < \phi_c, \tag{8}$$

marks a hybrid symmetric/centrifugal/inertial instability. Here $\phi_c = \tan^{-1}(-1 - \zeta/f)$ is the critical balanced Richardson angle. Figure 10 summarizes the depth-along-track calculation of the ϕ_{Ri_b} into a single time series by presenting

Fig. 9 Along-track sections of **a** squared horizontal buoyancy gradient ($|\nabla_h b|^2$), **b** vertical buoyancy gradient ($\nabla_z b$), **c** PV and **d** frontogenesis function (F_{front}). The white and black contours indicate mixed layer depth. The gray shadings show April 29, May 2, and May 3. The x-axis is as per Fig. 5
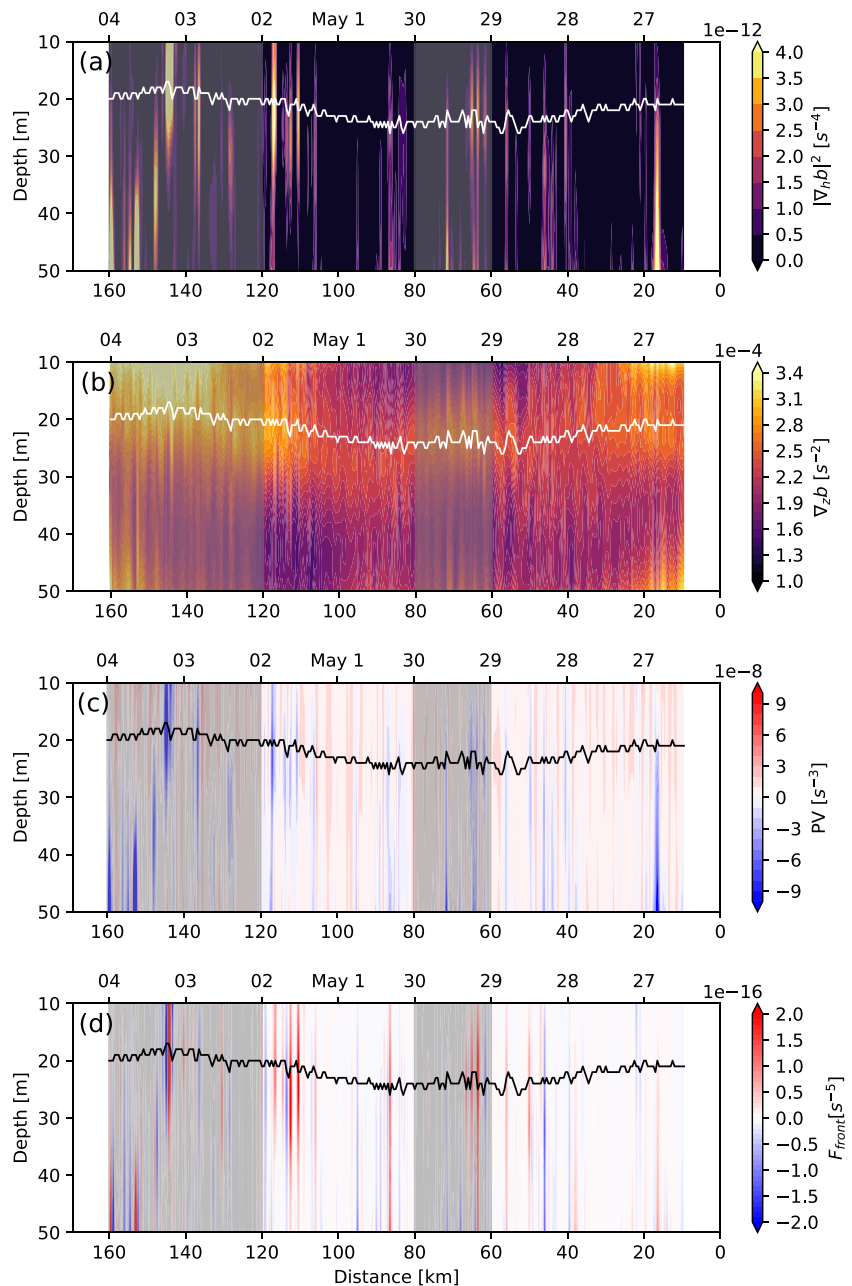
the fraction of the mixed layer where $q_{Obs} < 0$. During the observation period, we frequently observe conditions conductive to SI that account for more than 50%, consistent with the distribution of PV. In comparison, there is no obvious signal of gravitational instability, or a hybrid instability in Fig. 10, which implies that the external condition in late spring is somewhat quiescent, and no abrupt events (e.g., surface cooling) take place during this specific period.

While SI modifies the near-surface buoyancy field toward a $O(1)$ Ri_b, horizontal buoyancy gradients may persist once the system becomes marginally stable to SI. In the next, we examine another two processes that impact the stratification

in the upper ocean: baroclinic instability (BCI) and surface wind forcing. BCI injects potential energy into the mixed layer and drives substantial restratification (Boccaletti et al. 2007). On the other hand, down-front wind drives Ekman flow and advects dense water over light one, and triggers convection in the mixed layer (Thomas 2005). Analogous to surface fluxes (Mahadevan et al. 2012), we express the equivalent BCI flux as

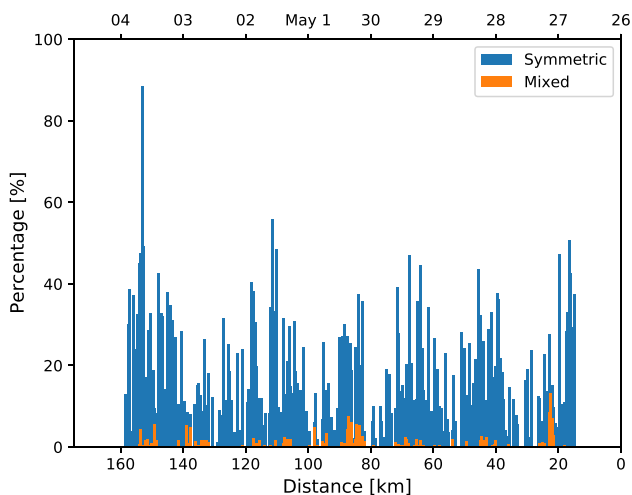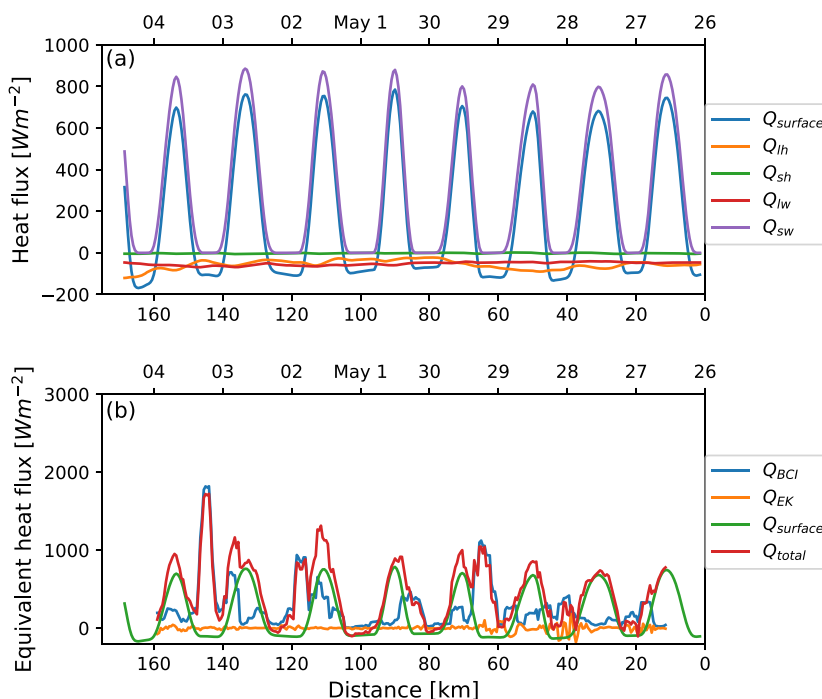$$Q_{BCI} = 0.06 \frac{b_x^2 H^2}{f} \frac{C_p \rho_0}{\alpha g}, \tag{9}$$

Fig. 10 Instabilities in the observation. The bars represent the percentage of the mixed layer that shows conditions favorable to SI and mixed instability. The x-axis is as per Fig. 4

where H is MLD, C_p is specific heat of seawater, and α is thermal expansion coefficient. The equivalent Ekman buoyancy flux (EK) is

$$Q_{EK} = -\frac{b_x \tau^y}{f} \frac{C_p}{\alpha g},$$ (10)

where τ^y is cross-track wind stress.

During the observational period, the surface heat flux Q_{surface} is dominated by the short-wave component and depicts positive/negative value in the daytime/night (Fig. 11a). The equivalent heat flux coming from the freshwater forcing is much smaller during this period (not shown). Summing Q_{surface}, Q_{BCI}, and Q_{EK} to arrive at a total surface buoyancy forcing Q_{total} indicates a persistent positive buoyancy forcing with frequent strong restratification events mainly due to BCI (Fig. 11b). Compared to Q_{surface}, changes in the surface stratification arising from Q_{BCI} and Q_{EK} are more intermittent in time. Q_{EK} takes both signs, reflecting downfront and upfront wind orientations, whereas Q_{BCI} illustrates an equivalent heat flux that is always positive. In addition to the abruptness of these features, magnitude of Q_{BCI} is frequently larger than the surface heat flux. BCI generates surface forcing amplitude in excess of surface heat flux on April 29, May 2, and May 3 with equivalent fluxes 1000 W/m^2, confirming the dominant submesoscale effect on stratification. It is noted that Q_{BCI} in our observation is comparable to that in North Atlantic during winter where the surface flux is much stronger and MLD is much deeper (Thompson et al. 2016). This may be caused by the difference of resolution between two observations. To test the hypothesis, a 4 km (8 points) average are applied to the glider-derived data. The resultant magnitude of Q_{BCI} is then found to be less than 500 W/m^2 (not shown). Therefore, our results call for a proper representation of submesoscale processes in the observation and next generation of ocean models.

Fig. 11 **a** Surface heat flux (Q_{surface}) induced by short wave (Q_{sw}), long wave (Q_{lw}), sensible (Q_{sh}), and latent (Q_{lh}) components. **b** Submesoscale overturning (Q_{total}) due to BCI (Q_{BCI}), wind-driven Ekman process (Q_{EK}), and surface heat flux (Q_{surface}). The data is smoothed by applying a 7-point running mean before plotting. The x-axis is as per Fig. 5

4 Summary and discussions

Based on a submesoscale-resolving glider observation, characteristics and underlying dynamics of submesoscale variability on an edge of Kuroshio shedding eddy in the northern SCS during spring are explored in this study. The major results of this study are summarized as follows:

- The spectral of the potential energy is characterized by a k^{-2} slope on the edge of the shedding eddy, indicating the existence of submesoscale instability.
- A distinct evolution in the type of instabilities occurring in regions of negative PV is revealed associated with strong lateral gradient of buoyancy. Conditions conducive to SI are rampant during the observation, though the MLD is shallow.
- Based on existing parameterizations, BCI plays an important role in the mixed layer restratification.

This study investigates the vigorous submesoscale motions on the edge of Kuroshio-originating eddy in the north SCS, which sheds light on the understanding of eddy dissipation. It should be noted that there are some uncertainties in our evaluation with two-dimensional data obtained from gliders. Even though we have adopted fast-sampling tactic in the 9-day observation, tidal signals are still difficult to be removed because internal tides superimpose upon each other and create and interference pattern (Rainville et al. 2010). The depth-averaged currents are not perfectly representative of flows in the mixed layer, which prevents us from establishing fine structures relative to velocity measurements (Todd et al. 2017). The gliders' tracks do not perpendicular to the front orientation strictly. With this in mind, the calculated PV may be underestimated. Moreover, our observations only print a general picture of submesoscale processes within shallow MLD; more efforts should be devoted to detailed dynamics at submesoscale through diverse observational approaches in the future.

Data availability The CMEMS, MUR, ETOPO1, ERA-5, QuikSCAT, ICOADS, and SODA products are available through the URLs: https://marine.copernicus.eu, https://podaac.jpl.nasa.gov, https://www.ngdc.noaa.gov, https://www.ecmwf.int, http://www.remss.com, https://rda.ucar.edu, and https://apdrc.soest.hawaii.edu, respectively. The data used in this study can be acquired from the Open Science Framework at https://doi.org/https://doi.org/10.17605/OSF.IO/H7Q83.

Code availability Codes for the paper can be available from corresponding author.

Declarations

Conflict of interest The authors declare no competing interests.

References

Boccaletti G, Ferrari R, Fox-Kemper B (2007) Mixed layer instabilities and restratification. J Phys Oceanogr 37:2228–2250. https://doi.org/10.1175/JPO3101.1

Callies J, Ferrari R (2013) Interpreting energy and tracer spectra of upper-ocean turbulence in the submesoscale range (1–200 km). J Phys Oceanogr 43:2456–2474. https://doi.org/10.1175/JPO-D-13-063.1

Cao H, Fox-Kemper B, Jing Z (2021) Submesoscale eddies in the upper ocean of the Kuroshio Extension from high-resolution simulation: energy budget. J Phys Oceanogr 51:2181–2201. https://doi.org/10.1175/JPO-D-20-0267.1

Chen G, Gan J, Xie Q, et al (2012) Eddy heat and salt transports in the South China Sea and their seasonal modulations. J Geophys Res: Oceans 117: https://doi.org/10.1029/2011JC007724

Dong J, Fox-Kemper B, Zhang H, Dong C (2020) The scale of submesoscale baroclinic instability globally. J Phys Oceanogr 50:2649–2667. https://doi.org/10.1175/JPO-D-20-0043.1

Dong J, Fox-Kemper B, Zhu J, Dong C (2021) Application of symmetric instability parameterization in the coastal and regional ocean community model (CROCO). J Adv Model Earth Syst 13:e2020MS002302. https://doi.org/10.1029/2020MS002302

Dong J, Fox-Kemper B, Jing Z et al (2022) Turbulent dissipation in the surface mixed layer of an anticyclonic mesoscale eddy in the South China Sea. Geophys Res Lett 49:e2022GL100016. https://doi.org/10.1029/2022GL100016

du Plessis M, Swart S, Ansorge IJ, Mahadevan A (2017) Submesoscale processes promote seasonal restratification in the Subantarctic Ocean. J Geophys Res: Oceans 122:2960–2975. https://doi.org/10.1002/2016JC012494

Erickson ZK, Thompson AF (2018) The seasonality of physically driven export at submesoscales in the Northeast Atlantic Ocean. Global Biogeochem Cycles 32:1144–1162. https://doi.org/10.1029/2018GB005927

Garabato ACN, Yu X, Callies J et al (2022) Kinetic energy transfers between mesoscale and submesoscale motions in the open ocean's upper layers. J Phys Oceanogr 52:75–97. https://doi.org/10.1175/JPO-D-21-0099.1

Garau B, Ruiz S, Zhang WG et al (2011) Thermal lag correction on Slocum CTD glider data. J Atmos Oceanic Tech 28:1065–1071. https://doi.org/10.1175/JTECH-D-10-05030.1

Hoskins BJ (1974) The role of potential vorticity in symmetric stability and instability. Q J R Meteorol Soc 100:480–482. https://doi.org/10.1002/qj.49710042520

Hoskins BJ (1982) The mathematical theory of frontogenesis. Annu Rev Fluid Mech 14:131–151. https://doi.org/10.1146/annurev.fl.14.010182.001023

Johnston TMS, Rudnick DL, Alford MH et al (2013) Internal tidal energy fluxes in the South China Sea from density and velocity measurements by gliders. J Geophys Res: Oceans 118:3939–3949. https://doi.org/10.1002/jgrc.20311

Kara AB, Rochford PA, Hurlburt HE (2000) An optimal definition for ocean mixed layer depth. J Geophys Res: Oceans 105:16803–16821. https://doi.org/10.1029/2000JC900072

Liu F, Wang Y, Wu Z, Wang S (2017) Motion analysis and trials of the deep sea hybrid underwater glider Petrel-II. China Ocean Eng 31:55–62. https://doi.org/10.1007/s13344-017-0007-4

Mahadevan A, D'Asaro E, Lee C, Perry MJ (2012) Eddy-driven stratification initiates north Atlantic spring phytoplankton blooms. Science 337:54–58. https://doi.org/10.1126/science.1218740

McWilliams JC (2016) Submesoscale currents in the ocean. Proc R Soc A: Math Phys Eng Sci 472:20160117. https://doi.org/10.1098/rspa.2016.0117

McWilliams JC (2021) Oceanic frontogenesis. Ann Rev Mar Sci 13:227–253. https://doi.org/10.1146/annurev-marine-032320-120725

Molemaker MJ, McWilliams JC, Yavneh I (2005) Baroclinic instability and loss of balance. J Phys Oceanogr 35:1505–1517. https://doi.org/10.1175/JPO2770.1

Munk W, Armi L, Fischer K, Zachariasen F (2000) Spirals on the sea. Proc R Soc Lond Ser A: Math Phys Eng Sci 456:1217–1280. https://doi.org/10.1098/rspa.2000.0560

Nan F, Xue H, Chai F et al (2011) Identification of different types of Kuroshio intrusion into the South China Sea. Ocean Dyn 61:1291–1304. https://doi.org/10.1007/s10236-011-0426-3

Nan F, Xue H, Yu F (2015) Kuroshio intrusion into the South China Sea: a review. Prog Oceanogr 137:314–333. https://doi.org/10.1016/j.pocean.2014.05.012

Nikurashin M, Vallis GK, Adcroft A (2013) Routes to energy dissipation for geostrophic flows in the Southern Ocean. Nat Geosci 6:48–51. https://doi.org/10.1038/ngeo1657

Qu T, Du Y, Gan J, Wang D (2007) Mean seasonal cycle of isothermal depth in the South China Sea. J Geophys Res: Oceans 112. https://doi.org/10.1029/2006JC003583

Rainville L, Johnston TMS, Carter GS et al (2010) Interference Pattern and Propagation of the M2 Internal Tide South of the Hawaiian Ridge. J Phys Oceanogr 40:311–325. https://doi.org/10.1175/2009JPO4256.1

Rainville L, Lee CM, Rudnick DL, Yang K-C (2013) Propagation of internal tides generated near Luzon Strait: observations from autonomous gliders. J Geophys Res: Oceans 118:4125–4138. https://doi.org/10.1002/jgrc.20293

Rudnick DL (2016) Ocean research enabled by underwater gliders. Ann Rev Mar Sci 8:519–541. https://doi.org/10.1146/annurev-marine-122414-033913

Rudnick DL, Cole ST (2011) On sampling the ocean using underwater gliders. J Geophys Res 116:C08010. https://doi.org/10.1029/2010JC006849

Sen A, Scott RB, Arbic BK (2008) Global energy dissipation rate of deep-ocean low-frequency flows by quadratic bottom boundary layer drag: computations from current-meter data. Geophys Res Lett 35. https://doi.org/10.1029/2008GL033407

Shchepetkin AF, McWilliams JC (2005) The regional oceanic modeling system (ROMS): a split-explicit, free-surface, topography-following-coordinate oceanic model. Ocean Model 9:347–404. https://doi.org/10.1016/j.ocemod.2004.08.002

Shchepetkin AF, McWilliams JC (2011) Accurate Boussinesq oceanic modeling with a practical, "stiffened" equation of state. Ocean Model 38:41–70. https://doi.org/10.1016/j.ocemod.2011.01.010

Swart S, Thomalla SJ, Monteiro PMS (2015) The seasonal cycle of mixed layer dynamics and phytoplankton biomass in the Sub-Antarctic Zone: a high-resolution glider experiment. J Mar Syst 147:103–115. https://doi.org/10.1016/j.jmarsys.2014.06.002

Swart S, du Plessis MD, Thompson AF et al (2020) Submesoscale fronts in the antarctic marginal ice zone and their response to wind forcing. Geophys Res Lett 47:e2019GL086649. https://doi.org/10.1029/2019GL086649

Taylor JR, Thompson AF (2023) Submesoscale dynamics in the upper ocean. Ann Rev Fluid Mech 55:null. https://doi.org/10.1146/annurev-fluid-031422-095147

Thomas LN (2005) Destruction of potential vorticity by winds. J Phys Oceanogr 35:2457–2466. https://doi.org/10.1175/JPO2830.1

Thomas L, Ferrari R (2008) Friction, frontogenesis, and the stratification of the surface mixed layer. J Phys Oceanogr 38:2501–2518. https://doi.org/10.1175/2008JPO3797.1

Thomas LN, Taylor JR, Ferrari R, Joyce TM (2013) Symmetric instability in the Gulf Stream. Deep Sea Research Part II: Topical Studies in Oceanography 91:96–110. https://doi.org/10.1016/j.dsr2.2013.02.025

Thompson AF, Lazar A, Buckingham C et al (2016) Open-ocean submesoscale motions: a full seasonal cycle of mixed layer instabilities from gliders. J Phys Oceanogr 46:1285–1307. https://doi.org/10.1175/JPO-D-15-0170.1

Thomsen S, Kanzow T, Colas F et al (2016) Do submesoscale frontal processes ventilate the oxygen minimum zone off Peru? Geophys Res Lett 43:8133–8142. https://doi.org/10.1002/2016GL070548

Todd RE, Rudnick DL, Sherman JT et al (2017) Absolute Velocity Estimates from Autonomous Underwater Gliders Equipped with Doppler Current Profilers. J Atmos Oceanic Technol 34:309–333. https://doi.org/10.1175/JTECH-D-16-0156.1

Viglione GA, Thompson AF, Flexas MM et al (2018) Abrupt transitions in submesoscale structure in southern drake passage: glider observations and model results. J Phys Oceanogr 48:2011–2027. https://doi.org/10.1175/JPO-D-17-0192.1

Wang D, Xu H, Lin J, Hu J (2008) Anticyclonic eddies in the northeastern South China Sea during winter 2003/2004. J Oceanogr 64:925–935. https://doi.org/10.1007/s10872-008-0076-3

Yang Q, Zhao W, Liang X et al (2017) Elevated mixing in the periphery of mesoscale eddies in the South China Sea. J Phys Oceanogr 47:895–907. https://doi.org/10.1175/JPO-D-16-0256.1

Yang Y, Wang D, Wang Q et al (2019) Eddy-induced transport of saline kuroshio water into the northern South China Sea. J Geophys Res: Oceans 124:6673–6687. https://doi.org/10.1029/2018JC014847

Yu X, Garabato ACN, Martin AP et al (2019) An annual cycle of submesoscale vertical flow and restratification in the upper ocean. J Phys Oceanogr 49:1439–1461. https://doi.org/10.1175/JPO-D-18-0253.1

Yuan D, Han W, Hu D (2006) Surface Kuroshio path in the Luzon Strait area derived from satellite remote sensing data. J Geophys Res: Oceans 111: https://doi.org/10.1029/2005JC003412

Zeng L, Wang D (2017) Seasonal variations in the barrier layer in the South China Sea: characteristics, mechanisms and impact of warming. Clim Dyn 48:1911–1930. https://doi.org/10.1007/s00382-016-3182-8

Zhang Z, Tian J, Qiu B et al (2016) Observed 3D structure, generation, and dissipation of oceanic mesoscale eddies in the South China Sea. Sci Rep 6:24349. https://doi.org/10.1038/srep24349

Zhang Z, Zhao W, Qiu B, Tian J (2017) Anticyclonic eddy sheddings from Kuroshio loop and the accompanying cyclonic eddy in the northeastern South China Sea. J Phys Oceanogr 47:1243–1259. https://doi.org/10.1175/JPO-D-16-0185.1

Zhang J, Zhang Z, Qiu B et al (2021) Seasonal modulation of sub-mesoscale kinetic energy in the upper ocean of the northeastern South China Sea. J Geophys Res: Oceans 126:e2021JC017695. https://doi.org/10.1029/2021JC017695

Zhong Y, Bracco A, Tian J et al (2017) Observed and simulated sub-mesoscale vertical pump of an anticyclonic eddy in the South China Sea. Sci Rep 7:44011. https://doi.org/10.1038/srep44011